Unbalanced response to growth variations reshapes the cell fate decision landscape

Jingwen Zhu[1]†, Pan Chu[1,2]†, Xiongfei Fu[1,2]*

Affiliations:

[1]CAS Key Laboratory for Quantitative Engineering Biology, Shenzhen Institute of Synthetic Biology, Shenzhen Institutes of Advanced Technology, Chinese Academy of Sciences, Shenzhen 518055, China

[2]University of Chinese Academy of Sciences, Beijing 100049, China

†These authors contributed equally: Jingwen Zhu, Pan Chu.

***Corresponding author:** Xiongfei Fu

Email: xiongfei.fu@siat.ac.cn

Author Contributions: Conceptualization: J.Z., P.C., and X.F.; Methodology: J.Z., P.C., and X.F.; Investigation: J.Z., and P.C.; Funding acquisition: J.Z., and X.F.; Writing – original draft: J.Z., P.C., and X.F.; Writing – review & editing: J.Z., P.C., and X.F.; Supervision: X.F.; Project administration: X.F.

Competing Interest Statement: The authors declare no competing interests.

Abstract

Cell-fate determination involves multiple layers of gene regulatory networks, whereas gene expression is globally modulated by cell growth regardless of specific regulations. Here, we utilize fundamental topology of mutual repression that allows a phenotypic bistability, to examine how such global regulation would affect the stability of phenotypic landscape and the accompanying dynamics of cell-fate determination. We show that the landscape experiences a growth-rate induced bifurcation between monostability and bistability. Theoretical and experimental analyses reveal that this bifurcating deformation of landscape arises from the unbalanced response of gene expression to growth variations. The path of growth transition across the bifurcation would reshape cell-fate decisions. These results illustrate that cell growth-rate, as a global characteristic of cellular physiology, plays a crucial role in cell-fate determinations.

Introduction

Cell fate determination is a ubiquitous and important process in living systems, enabling cells to transit to different, functionally important, and heritable states in the absence of genetic variations(1, 2). Classical theory proposed by Waddington(3) depicts the developmental process as a ball rolling down the epigenetic landscape with 'hills' and 'valleys', of which the 'valleys' define the phenotypic states that the cells can access. Rather than this deterministic picture, recent studies have discovered that cell fate is flexible and reversible, such that differentiated cells could be rejuvenated to pluripotent state or directly jump from one 'valley' to the other(4-6). As such, cell fate specifications can be interpreted as the mechanism by which cells make choices in the bifurcation landscape governed by the complex gene regulatory networks(7, 8). These networks determine the phenotypes of cells by controlling changes in gene expression through the activities of the transcription factors(9-11), and extrinsic constraints like elaborate signaling dynamics and environmental cues(12, 13). Therefore, understanding the process of cell fate determinations requires to describe the integrative impact of both activities of transcription factors and extrinsic parameters on the cell fate decision landscape, as well as the underlying mechanisms.

It's noteworthy that gene expression of transcription factors, besides specific regulation, also exhibits a strong dependence on the physiology of cells (e.g., cell growth rate). Prominent examples are found in both microorganisms and multicellular systems, such as lysis-lysogeny decision of bacteriophage lambda infecting by fluctuations of gene expression rate coupled with cell physiological state(14, 15), proliferation-to-invasion transition of *Bacillus subtilis* in response to the nutrient limitation(16, 17), and epithelial–mesenchymal transition (EMT) controlling by surrounding niches(18-20). It's still a lack of direct evidence how such global regulation of cellular physiology would introduce adaptations in gene regulatory networks and distort the cell fate decision landscape.

In this work, using *Escherichia coli* as a model system, we implemented a mutually repressive synthetic circuit(21-23), characterized as a fundamental gene network that shapes a binary decision-making landscape(7, 11), to examine how its cell fate decision landscape would response to growth variations and the accompanying dynamics of cell-fate determination. Pioneering bacterial physiology studies have demonstrated the global interdependence between gene expression and cell growth due to the re-allocation of cellular resources (e.g., building blocks, machinery for transcription and translation) and the adaption of metabolic networks(24-32). Our results reveal that the global coordination is not equal over the regulatory network. The unbalanced responses in the two mutually repressive genes induce the bifurcating deformation of the fate-decision landscape. This reshaping process does not depend on specific molecular signaling or regulation, but an intrinsic characteristic of cell physiological regulation upon the fate determination networks.

Results

Growth-rate dependent phenotypic bistability

We introduced a well-established genetic circuit with a mutually repressive topology composed of two transcription factors (TFs), LacI (controlled by P_L*tetO-1* promoter) and TetR (controlled by *Ptrc2* promoter) (21-23) into *E. coli* cells This system can display two mutually repressive states by two distinct reporters, the green fluorescent protein GFPmut2 (GFP) and the red fluorescent protein mCherry (RFP), respectively (Fig. S1A). During steady-state growth in a nutrient-rich growth medium (e.g., SOB, see Materials and Methods), cells can be induced to two distinct phenotypes (i.e., green state: high LacI/GFP expression; red state: high TetR/RFP expression) by the respective inducer, and maintain the same state for a long time even after removal of inducer (Fig. S1B-C). This bistable phenomenon is known as hysteresis of the mutually repressive system.

Surprisingly, we noticed that the initial phenotypic state cannot be always maintained during the batch culture growth. For a population initialized in the green state, both GFP and RFP intensity increased at the later log phase when the growth rate slows down. Further decrease in growth rate promoted a developmental progression where the GFP signal dropped abruptly with a concomitant increase of the RFP signal. We followed this state transition dynamics by defining the phenotypic changes during nutrient depletion (Fig. S2). The ratio of cells in the green state monotonically decreased throughout cell culture, as the growth shifted from a balanced-growth phase to a nearly stationary phase (Fig. 1A). Eventually, all cells initially in the green state shifted to the red state, when the growth rate dropped accompanied by nutrient depletion (Fig. 1A upper panel). Time-series of single-cell fluorescent images over the growth curve more explicitly confirmed the phenotype transition from green state to red state (Fig. 1B). On the contrary, cells with an initial red state do not exhibit the state transition (Fig. 1A bottom panel). We confirmed that this transition is not a genotypic variation, as re-incubation of the

cells from the stationary phase to the fresh SOB medium can recapture the bistability (Fig. S2). Furthermore, cells incubated in the fresh SOB medium supplemented with conditioned medium collected from the stationary phase did not change their states, suggesting that the metabolic products generated during nutrient depletion do not contribute to the transition of cell phenotypes. Based on these observations, we hypothesized that the global physiology variations may underlie the reshaping of the cell fate decision landscape, implicating in the phenotype transition during growth rate decreases in batch culture growth.

Therefore, to validate the dependence of phenotype variations on cellular physiology, we examined the cell stable states under balanced exponential growth in different defined media to achieve various growth rates over an extensive range (Table S3). In these conditions, the global effects of physiology are reflected first and foremost by the growth rate(24, 26, 27) Cells were first fully induced to two respective states and kept growing exponentially via dilution regularly into fresh medium until steady state (Fig. 1C, details in Materials and Methods). Cells initialized as a red state can maintain the high red expression state over a wide range of growth rates (Growth rate λ from 1.60 h^{-1} to 0.18 h^{-1}, Table S5), with the fluorescent protein concentration increases as the growth rate decreases (red symbols in Fig. 1C, and Table S5). However, cells starting with high GFP expression can only maintain the state from fast- to moderate-growth conditions (λ from 1.61 h^{-1} to 0.59 h^{-1}, green symbols in Fig. 1C, and Table S5). When steady-state growth rate was inferior to approximately 0.5 h^{-1}, all green state cells switched to red state (green square and green triangle in Fig. 1C), suggesting the loss of bistability. We further demonstrated that the system exhibits a large range of hysteresis in a fast-growth medium (Fig. S3A-B), but almost null of hysteresis in slow growth condition (Fig. S3C-D), thereby confirming the loss of bistability. Additionally, we observed similar growth-rate dependence by growth rate titration via the translation-inhibiting antibiotic (Fig. S4). The interplay between the growth-mediated global effects and specific mechanisms of the

regulatory network may invoke unintended interactions, e.g., the growth modulation of gene expression(25), growth feedback(33), and growth retardation caused by metabolic burden(34). Our experiments showed no significant difference in growth rates between the two distinct phenotypes (Fig. 1C right panel, and Table S5). Thus, the variation of phenotypes for this mutual repressive system is not induced by the nonlinear dilution due to the metabolic burden caused by gene expression. These results lead us to expect that, the cell fate determination might take place without complex regulation and biochemical signaling.

The unbalanced response of gene expression to growth-rate variations

To further elucidate how cellular physiology is involved in reshaping the fate decision landscape, we quantitatively examined the growth-rate-dependent global effects on gene expression of the mutually repressive circuit. We separated the circuit into two constitutively expressed parts (i.e., *Ptrc2*-driven *tetR* and P_L*tetO-1*-driven *lacI*, Fig. S5A) and characterized the corresponding expression capacities(35) (denoted as $\tilde{\alpha}_{R,G}$ in Fig. S6, defined as the constitutively expressed protein concentration under balanced exponential growth) by quantifying the fused fluorescent signals under various growth conditions. As shown in Fig. 2A, the expression capacities exhibit a strong growth rate-dependent effect. Both expression capacities increase faster than $1/\lambda$ as growth rate decreases (Fig. S5B), indicating that additional global regulation other than the cell volume variations in changing growth rate could be significant (see SI). Notably, the ratio of expression capacity at different growth rates, $\tilde{\alpha}_R/\tilde{\alpha}_G$, indicates the unbalanced variation of two proteins in response to the growth rate changes (Fig. S5C): an approximately doubled increase in the ratio from fast- to slow-growth conditions. We further validated the unbalanced variations of two repressive genes by examining the mRNA abundance. The transcriptomics (mRNA-sequencing, see SI) confirmed unequal dependence on growth-rate in the expression capacities of two regulators (Fig. S5D and S5E). Using an empirical dependence of translation activity on growth-rate(24-26, 30), we

calculated the effective protein synthesis rates (denoted as $\alpha_{R,G}$ in Fig. S6). The theoretical prediction can recapture the experimentally measured protein synthesis rates, of which there are maximums around the moderate growth rates ($\lambda_m \approx 0.5$ h^{-1} for α_R and $\lambda_m \approx 0.75$ h^{-1} for α_G; Fig. S5F and S5G). Therefore, although the expression capacities and synthesis rates of both sides in the mutually repressive circuit show the same trend of dependence on the growth rate, their detailed degree of dependence are not equal, which would break the balance of the mutual repression.

To study the consequence of these unbalanced variations of gene expression under different growth-rate conditions, we constructed a minimal model to describe the mutually repressive circuit, considering the growth-dependent global gene regulation (see SI and Fig. S6). The model predicts that the stable steady-states of the system are determined by the intersection of two nullclines(36, 37) (solid lines in Fig. 2B) defined by the repressive regulatory functions (Fig. S6). By nondimensionalized analysis, we found the dimensionless repression thresholds of the nullclines (normalized by their expression capacities and denoted as $\widetilde{K}_{DR,DG}$) decrease steadily as growth rate decreases (Fig. 2C). However, the growth-rate-induced shifts are not balanced for the two repressive thresholds. As a result, the number of possible intersections of the two nullclines changes in different growth rates, yielding the variations in available states of the system (from bistable to monostable, from solid lines to transparent lines as illustrated in Fig. 2B). Our analysis suggested that although it has been demonstrated that this mutually repressive circuit is robust to growth-mediated dilution(33) the unbalanced dependence of gene expression on growth-rate would impose a phase transition of available phenotypic states on the system (Fig. S7)(25).

The phase transition can be more explicitly illustrated by the quasi-potential landscape (Fig. 2D, and SI), of which the local minima represent the stable phenotypic states of the system(38-

40). The calculated quasi-potential landscape exhibits a single minimum with highly expressed TetR/RFP in slow-growth conditions. As the growth rate increases, the landscape bifurcates into two local minima (the original one in the red state and the other new minimum in the green state), suggesting the system becomes bistable and hysteretic. Further increase in growth rate would impose the other saddle-node bifurcation, effectively leading to destabilization of the red state. Therefore, the growth rate plays a role as a global control parameter(41) to induce two bifurcation points from a monostable state to a bistable one, and further to the other monostable state. The above experiments only captured one bifurcating point from the bistable phase of either green or red state to the monostable phase of a single red state as the growth rate decreases (colored symbols in Fig. 2D). Another bifurcation from a green monostable state to bistability requires faster growth that is not biologically accessible in our system.

The determination of the critical growth-rate of bifurcation

Further analysis of the model suggests that the bifurcation points would shift as the variations in the repression thresholds (i.e., K_{DR} and K_{DG}, see Fig. S6), which is governed by the equilibrium dissociation constant of the repressor from its corresponding binding operator(42). Here, we constructed several modified LacI binding sites to obtain different dissociation constants (Fig. 3A, and Fig. S8). Such designs enable us to vary the repression threshold K_{DG} without affecting the Hill coefficient (cooperativity) of the regulatory function ($H_G(R)$ in fig. S6). We quantified the repression thresholds K_{DG} for the modified circuits (Fig. 3A). Compared with the original circuit LO1, the two modified circuits exhibit a smaller *lac* operator dissociation constant (i.e., higher LacI binding affinity to their binding sites).

We further characterized the bifurcation diagrams of the modified circuits under different growth-rate conditions. Consistent with the model prediction, the circuits with different repression thresholds exhibit a shift of bifurcation points (Fig. 3B). Specifically, compared with

the LO1 circuit that bifurcates from a monostable red state to bistable as the growth rate increases (Fig. 3B, LO1), the circuit with a smaller dissociation constant K_{DG} (i.e., with higher binding affinity) can maintain bistability over the wide range of growth rates (Fig. 3B, LO2), suggesting it's a robust design for "toggle switch" regardless of variations in growth rates. Further reduction of K_{DG} leads the system becomes monostable (green state) for fast growth rate (λ > 0.5 h^{-1}) and bistability under λ < 0.5 h^{-1} (Fig. 3B, LO3). The abovementioned experiments as well as the model demonstrated that the growth-mediated gene expression could reshape the phenotypic potential landscape, yielding the transition of states through bifurcation points by varying growth rates.

Growth-rate transition across the bifurcation point

Although the landscape deformation enables variations in phenotypes, it remains unclear how cell state is determined when the growth rate changes across the bifurcation points. According to Waddington's metaphor of cell fate decision, the activity of regulatory networks shapes the landscape and determines phenotypic states, while fate decision trajectories are more likely to traverse during development under varying environment(3, 41). To address this question, we characterized the dynamics of cell phenotype determination across the bifurcation point during growth down- and up-shift, by monitoring the averaged fluorescent protein concentrations of initial green state populations (Fig. 4A, see Materials and Methods for details). Accompany with growth shift, the cell state would change but along distinct trajectories depending on the landscape topology of the circuits (Fig. 4B).

For LO1 strain which has bistability at fast growth yet only red monostable state allowed at slow growth, cells initialized as the green state at fast growth condition experience a phenotypic state transition during growth downshift. For the first several generations after the downshift, both GFP and RFP concentrations increase (Fig. 4B LO1), because of a higher protein synthesis

rate with a slower growth-mediated dilution of protein throughout the growth down-shift. The further increase in TetR/RFP expression triggers the repression of LacI/GFP, promoting a temporal progression of cell state where the GFP signal drops with a concomitant increase of the RFP signal until the steady-state. The sequential growth up-shift starting with cells in the red state maintains the high TetR/RFP expression, suggesting the hysteresis and irreversibility properties. Alternatively, the LO3 strain retains its initial green state throughout the down- and up-shift (Fig. 4B LO3). During growth down-shift, both the GFP and RFP signals of LO3 strain increase and eventually reach the steady-state where GFP was highly expressed. Meanwhile, during the growth up-shift, the cell exhibits a reduction of both fluorescent signals, but not a complete reversible trajectory as that of down-shift. The reduction rate of both GFP and RFP signals is fast initially and decays, exhibiting a strong correlation with the kinetics of growth rate(31). Similar correlated dynamics can also be observed in LO1 strain with an initial red phenotype during the growth down- and up-shift (Fig. S11). With a quasi-equilibrium assumption that the effective synthesis rates $\tilde{\alpha}_{R,G}$ are determined by the instantaneous growth rate $\lambda(t)$, our mechanistic model (Fig. S6, and SI) can recapture the main dynamic features of the state transition driven by growth shift (Fig. S12). Therefore, besides the direct constraint by the defined regulatory network, the dynamics of cell state transition also depend on the kinetics of growth transition.

Our deterministic model integrating the gene regulatory network with the global physiological constraints provides mechanistic insight into how growth variations could reshape the landscape and navigate cell-fate determination. However, this deterministic interpretation still encounters several challenges to describe the details of cell state transition dynamics during growth shift. For example, the growth shift between two bistable landscapes without bifurcation (e.g., LO2 strain) would induce the bimodal gene expression (Fig. 4B LO2). During the growth down-shift, the population of LO2 strains in the green state first went through a co-

activation of both side genes of the mutual repression, and then split into two groups: one stays in the co-activation of both genes (dots in Fig. 4B LO2), and the other one in high TetR/RFP state with LacI/GFP repressed (circles in Fig. 4B LO2). We hypothesized that the co-activation state is because the potential landscape has a shallow barrier (Fig. 4B LO2), such that noise in the gene network could aid and trigger the hopping between the two "valleys", resulting in a bimodal distribution of the gene expression level in an isogenous population(43, 44) Meanwhile, the following growth up-shift drove the two groups of cells into mutually repressive states where only one side of the gene is highly expressed. Further detailed examination of single-cell lineage tracing(45-48) is required to address how and to what extent the stochasticity of the gene expression affects the cell commitment during the landscape deformation induced by growth shift(44). Here, with experimental relevant parameters of noise, we introduced a stochastic scene into our model, thereby recapturing the potential landscapes(49, 50) (SI and Fig. S13).

Discussion

Classical developmental studies consider the deformation of Waddington's landscape that varies the number of cell fate choices is usually induced by the upstream signaling, thereby driving the dynamics of cell differentiations(51-53). Cell differentiation always exhibits a correlation between cell-phenotype transition and growth-rate variations. Prominent examples include the transition between epithelial and mesenchymal cells (EMT)(18-20) and the proliferation-to-invasion transition of *B. subtilis*(54). However, the cause-and-effect relationship between two processes is always hard to distinguish in these natural systems(55). The reconstitution by synthetic biology provides a complementary but important approach to recapitulate the fate decision processes with a fundamental set of regulations and enables the quantitative examinations of key parameters under well-controlled conditions(56-59). This study, using a simple mutually repressive circuit as an example, demonstrated that global regulation of growth-rate on the gene expression would break the balance of the regulatory network, thereby distorting the phenotypic landscape and further shaping the cell-fate determination. It is noteworthy to revisit the role of growth variations in the spatiotemporal cell differentiation(43, 57, 60).

Materials and Methods

Stains and construction

All experiments were done using strains derived from Escherichia coli K-12 NCM3722 background. The strain E. coli NCM3722 was a gift from Dr. Chenli Liu. Strains derived from the wild-type strain are listed in Table S1. Modified strains are edited by Lambda-Red recombination (pSIM series plasmids(61)) with polymerase chain reaction (PCR) amplified homologous fragments marked with antibiotic resistance genes, and drug marker was eliminated by Cre mediated site-specific recombination. All mutual repression circuits were derived from pECJ3 plasmid (gift from Dr. James Collins(22, 23), Addgene plasmid # 75465). Genetic circuits are harboring in plasmid with ColE1 origin. Genetic parts, including promoter, ribosome binding sites (RBS) and coding sequence were amplified from pECJ3 by PCR. Small parts which less than 200 bp were assembled via oligos (GENEWIZ Guangzhou Lab). Purified DNA fragments were assembled by One Step Cloning Kit (Vazyme Co., Ltd. Cat. C113) or Golden gate assembly(62) (NEB, Cat. M0202 and R3733). Sequence contents of genetic parts are collected in Table S10.

Growth media

Quantitative experiments were performed in MOPS buffered defined medium(63) supplemented with the appropriate antibiotic, i.e., 10 μg/mL kanamycin (Aladdin K103024), to maintain the plasmids. The MOPS buffer contains 40 mM MOPS (Sigma-Aldrich V900306), 4 mM Tricine (Sigma-Aldrich V900412, adjusted to pH 7.4 with KOH), 0.01 mM $FeSO_4$, 0.276 mM K_2SO_4, 0.5 μM $CaCl_2$, 0.525 mM $MgCl_2$, 50 mM NaCl, 1.32 mM K_2HPO_4 and micronutrient mixtures (3 nM $(NH_4)_6Mo_7O_{24}$, 0.4 μM H_3BO_3, 30 nM $CoCl_2$, 10 nM $CuSO_4$, 80 nM $MnCl_2$, 10 nM $ZnCl_2$). Unless otherwise specified, our MOPS buffer contains 9.5 mM NH_4Cl as nitrogen source. Different growth rates were achieved by providing different compositions of nutrients including carbon and nitrogen sources. Detailed information on these

media is provided in Table S3 and S4. Various concentrations of mupirocin (Sangon Biotech A606674) were added to attain different growth rates by means of translation inhibition. The chemical inducers, IPTG (Sigma-Aldrich I6758, isopropyl β-D-1-thiogalactopyranoside) and cTc (Aladdin C103023, Chlorotetracycline hydrochloride) were diluted to appropriate working solution when necessary.

The nutrient-rich bacterial growth medium SOB (Sigma-Aldrich H8032, Hanahan′s Broth) contains 0.186 g/L KCl, 2.4 g/L $MgSO_4$, 0.5g/L NaCl, 20 g/L tryptone and 5g/L yeast extract. Cloning and genetic modifications used LB medium (HuanKai Microbial 028324, LB Broth without sugar), which contains 5 g/L NaCl, 10 g/L Tryptone, and 5 g/L yeast extract.

Cell culture and growth rate measurement

Unless otherwise specified, cell culture and growth rate measurements were carried out in 3 steps: seed culture, pre-culture and experimental culture. Strains were streak in LB agar plates from glycerol stocks. Cells were incubated at 37 ℃ for 10-12 hours. 3-5 colonies were picked from agar plate and inoculated into 14 mL tube containing 3 mL LB medium supplemented with an appropriate antibiotic. The culture was performed in a shaker (220 r.p.m., 37 ℃, Shanghai Zhichu Instrument) for at least 3 hours (or longer for cells with a slower growth rate) as seed culture. At the pre-culture step, cells were transferred to a 0.22 μm filter, and washed with a pre-warmed experimental medium (at least 3-fold the volume of the seed culture) to remove the remnants of LB medium. Washed cells were diluted into the experimental medium with a starting OD_{600} (optical density at 600nm, which was measured using a spectrophotometer Genesys 10s, Thermo Fisher Scientific) at approximately 0.01. Successive dilutions were achieved once OD_{600} reached 0.2 and repeated for several rounds to keep a balanced growth condition. Samples for further quantitative measurements were collected to an OD_{600} less than 0.2. Unless otherwise stated, pre-culture and experimental culture steps were

performed in a water-bath shaker (150 r.p.m., 37 °C, Shanghai Zhichu Instrument) in a 29 mm × 115 mm test tube with no more than 10 mL medium.

For the growth rate measurement, cells were kept in pre-culture steps for at least 10 generations to establish a steady-state growth. Experimental cultures were started by diluting the pre-culture to an OD_{600} of approximately 0.02. Five to eight points were measured within a range of OD_{600} from 0.03 to 0.2. The growth rate (λ) was calculated by fitting the data to an exponential growth curve.

Flow cytometry

The fluorescence intensity distribution of each sample was measured using a flow cytometer (CytoFLEX S, Beckman Coulter Life Sciences) with excitation/emission filters 488 nm/525 nm (FITC) for GFP (as well as sfGFP and mVenus) and 561 nm/610 nm (ECD) for mCherry. The gain for FSC, SSC, FITC and ECD channels were set to 500, 500, 250 and 1500, respectively. The trigger level was set manually on SSC-H according to different growth conditions. The flow rate was 60 μL/min and at least 50,000 events were recorded. The detected event number per second should be kept below 3000 events/second.

Characterization of fluorescence intensity per mass

Fluorescence intensity per mass was employed to monitor the relative protein concentration. 10 μL samples of each culture were diluted into 500 μL pre-cooled MOPS buffer containing 5 mg/mL kanamycin to arrest protein translation and cell growth, immediately. The GFP intensity per mass and RFP intensity per mass were calculated by customized parameters (fig. S14): 1000 × FITC-H/FSC-H (GFP intensity per mass) and 1000 × ECD-H/FSC-H (RFP intensity per mass). FSC-H was used to normalize the effect of cell size change in different growth conditions as its good linear relation with cell volume and cell mass(64). All samples were stored in ice for 18 hours before measuring for fully maturing the fluorescent proteins.

Protein synthesis rate measurement

Steady-state growth rate λ^* and relative protein concentration P^* were measured as mentioned above. For constitutively expressed protein, synthesis rate α was evaluated as:

$$\alpha = P^* \cdot \lambda^*$$

For instantaneous protein synthesis rate $\alpha(t)$ measurement, cells were collected and measured their relative protein concentration $P(t)$ and optical density $\mathrm{OD}(t)$, simultaneously. The $\alpha(t)$ can be inferred by the equation:

$$\alpha(t_i) = \frac{P(t_{i+1})\mathrm{OD}(t_{i+1}) - P(t_i)\mathrm{OD}(t_i)}{\left(\mathrm{OD}(t_{i+1}) - \mathrm{OD}(t_i)\right)\mathrm{OD}(t_i)}$$

Hysteresis experiment

Cells were kept growing exponentially for 10 generations (it takes usually ~ 4.5 h in RDM glucose medium and ~ 17 h in MOPS acetate medium) in the presence of 0.2 mM IPTG (to be triggered to red state) or 10 ng/mL cTc (to be triggered to green state). Cells were subsequently washed with a pre-warmed experimental medium to eliminate the inducers and diluted into a medium containing various concentrations of cTc within the range from 0 to 10 ng/mL for a further 10 generations. Samples were collected and detected using flow cytometer, 50,000 events were collected for each sample.

Response curve measurements

All fluorescent intensity measurements were taken from flow cytometry. For characterizing the response function of the promoter variates, pRS3.R11_lacI series and pK4.5_C8 series plasmids were constructed. The pRS3.R11_lacI series plasmid harbouring the nahR-Psali expression system(65) which can respond to the sodium salicylate (Sigma-Aldrich, S3007) were used to titrate the expression level of LacI, and the pRS3.R11_lacI-mVenus plasmid

expressing lacI-mvenus fusion version was used to measure the LacI expression level in a specific concentration of the sodium salicylate, i.e., the input of the response curve (see Fig. S8). Strain with blank plasmid pK4-Blank and pRS3.R11_mVenusn (mVenusn containing a C67Y mutation compared to wild type mVenus loses its chromophore) was used to measure the background fluorescent intensity. The promoter variates were inserted into the upstream of reporter gene mVenus in pK4.5_C8 plasmids for measuring the output of the response curve (see Fig. S8). The strains containing pRS3.R11_lacI and pK4.5_C8 plasmids were inoculated into RDM glucose medium supplied with proper antibiotics in 14 mL tube at 37 °C, 220 r.p.m. for at least 8 hours. Overnight cultures were adjusted to OD_{600} 0.2 by diluting with MOPS buffer. After OD adjustment, cultures were diluted by 150-fold into 149 μL RDM glycerol medium with antibiotics and specific sodium salicylate concentration. Cells were grown in a thermostatic microplate shaker (AOSHENG, MB100-4A) maintained at 37 °C and 1000 r.p.m., using flatten button 96-well-plates (Corning, 3336) and sealing with breathable film (Axygen, BF-400-S). After growing 7 generations, 15 μL cells were diluted into 135 μL pre-warmed fresh identical medium for 4 generations. 10 μL cultures were collected and diluted into 500 μL pre-chilled MOPS kanamycin buffer. All samples were stored in an ice slurry for 18 hours before the fluorescence intensity measuring.

Nutrient-shift experiment

The down-shift and up-shift experiments presented in Fig. 4, Fig. S10 and S11 were carried out between RDM glucose medium and MOPS(-NH_4Cl) glutamate glucose medium56. RDM glucose medium contains extra amino acids (EZ) and nucleotides (ACGU) which provides a fast growth rate. Before the growth down-shift, the culture was in exponential growth at 37 °C in RDM glucose medium. When OD_{600} reached 0.15, a dilution was performed with a dilution ratio of 1/10 to the pre-warmed MOPS(-NH_4Cl) glutamate glucose medium. Successive 1/5 dilutions to the same medium were applied once the OD_{600} reached approximately 0.15 to keep

the OD_{600} of culture between 0.03 to 0.15. The OD_{600} of the culture was measured frequently and an aliquot of cell suspension was taken at the same moment of OD_{600} measurement for further flow cytometry analysis immediately. When cells' fluorescence intensity levels varied less than 5% compared to the previous one, cells were considered to reach to steady-state. A growth upshift was subsequently carried out to RDM glucose medium using the same procedure as described in growth downshift until steady-state. The instantaneous growth rate was calculated as:

$$\lambda(t_i) = [\log_2 \mathrm{OD}(\mathrm{t_{i+1}}) - \log_2 \mathrm{OD}(\mathrm{t_i})]/(\mathrm{t_{i+1}} - \mathrm{t_i})$$

Cell Imaging

Cells were imaged using Nikon Ti-E microscope equipped with 100 × objective (NA=1.45). Illumination source was X-Cite 110LED, and Andor Zyla 4.2s sCMOS was used to capture images. Phase-contrast and widefield fluorescence images were acquired. Cell culture was adjusted to OD_{600} 0.1 before imaging. A 1.5% agarose pad with MOPS buffer was used to immobilize the cells. Inoculate 2 μL cell culture on a coverslip and cover by agarose pad gently. Each sample was collected and imaged within 5 min. For the green fluorescence channel, emission filter and excitation filter were FF02-482/18-25 and FF01-525/45-25 (Semrock), and the exposure time was 50 ms. For red fluorescence, emission and excitation filters are FF01-591/6-25 and FF01-647/57-25 (Semrock), and 100 ms exposure time.

mRNA sequencing and data processing

Samples used for RNA extraction was prepared following the method described in the main text. About 1 OD/mL cells were mixed with 2 volumes of RNAprotect Bacteria Reagent (Qiagen, 76506), and cell pellet was collected by centrifuging at 2500g for 8 minutes at room temperature. For long-term storage, collected samples were stored at -70 °C. Cells were destructed in TE buffer containing lysozyme (Sigma-Aldrich, 62917) and incubated at room

temperature for 5 min. After lysis procedure, total RNA was extracted from cell lysate by RNeasy Plus Mini Kit (Qiagen, 74136).

Total RNA which was carried out following the method described above was removed rRNA by rRNA Depletion Kit (Vazyme, N407-01), and cDNA library preparation and high-throughput sequencing were performed in MGI platform (BGI, Wuhan lab).

Sequencing raw data was processed using customed python scripts (https://github.com/MinTTT/RNA_seq_pip). Briefly, raw sequencing files were trimmed adapters using cutadapt(66). Next, the sequencing data was aligned to reference sequences using Bowtie2(67). The referencing sequences were generated according to the sample type, where the genome is NCM3722 (GenBank: CP011495.1) for all strains and the plasmids (pECJ3_lacI-sfgfp_delta_TetR or pECJ3_tetR-sfgfp_delta_LacI depending on the strains, the sequence details are listed in Table S3). After alignment, reads coverage over whole genome was calculated. Specifically, all properly mapped reads were separated according to their mapped strands using samtools(68). Notice, we have removed the reads mapped to tRNA regions considering the bias caused by non-uniform of tRNA in different samples(69).

mRNA abundance ϕ_i^m was calculated by followed equation,

$$\phi_{\mathrm{i}}^{\mathrm{m}} = 10^{-6} \cdot \mathrm{TPM}_i = \frac{\#_{\mathrm{i}}^{\mathrm{reads}}/\mathrm{l}_{\mathrm{i}}}{\sum_{\mathrm{j}} \#_{\mathrm{j}}^{\mathrm{reads}}/\mathrm{l}_{\mathrm{j}}}$$

where $\#_i^{\mathrm{reads}}$ represents the number of mapped reads of gene i, l_i denotes the length of gene i.

Acknowledgements

The authors thank C. Liu for sharing *E. coli* strain, X. Li, Y. Bai, S. Huang, C. Lou, F. Jin, C. Liu, C. He, Z. Ma for discussions, comments, and technical support.

Funding: This work is supported by the National Key R&D Program of China (Grant No. 2018YFA0903400), the National Natural Science Foundation of China (Grant No. 32071417), the Guangdong Basic and Applied Basic Research Foundation (Grant No. 2021A1515110863).

Data and materials availability: Sequencing data have been deposited to the NCBI BioProject with the accession code PRJNA835246. Major experimental data supporting the findings of this study are available within the main text and SI. Other data are available from the corresponding author on reasonable request. Custom-made simulation code is available via GitHub at https://github.com/Fulab-SIAT/cell_fate_2022.

References

1. G. Balázsi, A. van Oudenaarden, J. J. Collins, Cellular decision making and biological noise: from microbes to mammals. *Cell* **144**, 910-925 (2011).
2. J. M. Slack, L. Dale, *Essential developmental biology*. (John Wiley & Sons, 2021).
3. C. Waddington, *The Strategy of the Genes: A Discussion of Some Aspects of Theoretical Biology*. (London: Allen and Unwin, 1957).
4. K. Takahashi, S. Yamanaka, Induction of pluripotent stem cells from mouse embryonic and adult fibroblast cultures by defined factors. *Cell* **126**, 663-676 (2006).
5. J. Hanna *et al.*, Direct cell reprogramming is a stochastic process amenable to acceleration. *Nature* **462**, 595-601 (2009).
6. R. Ahrends *et al.*, Controlling low rates of cell differentiation through noise and ultrahigh feedback. *Science* **344**, 1384-1389 (2014).
7. E. H. Davidson, *The regulatory genome: gene regulatory networks in development and evolution*. (Elsevier, 2010).
8. I. S. Peter, E. H. Davidson, Assessing regulatory information in developmental gene regulatory networks. *Proc. Natl. Acad. Sci. USA.* **114**, 5862-5869 (2017).
9. K. S. Zaret, Pioneer transcription factors initiating gene network changes. *Annual review of genetics* **54**, 367 (2020).
10. P. Hayward, T. Kalmar, A. Martinez Arias, Wnt/Notch signalling and information processing during development. (2008).
11. J. X. Zhou, S. Huang, Understanding gene circuits at cell-fate branch points for rational cell reprogramming. *Trends Genet.* **27**, 55-62 (2011).
12. R. Iglesias-Bartolome, J. S. Gutkind, Signaling circuitries controlling stem cell fate: to be or not to be. *Current opinion in cell biology* **23**, 716-723 (2011).
13. E. Kussell, S. Leibler, Phenotypic diversity, population growth, and information in fluctuating environments. *Science* **309**, 2075-2078 (2005).
14. A. Arkin, J. Ross, H. H. McAdams, Stochastic kinetic analysis of developmental pathway bifurcation in phage λ-infected Escherichia coli cells. *Genetics* **149**, 1633-1648 (1998).
15. A. B. Oppenheim, O. Kobiler, J. Stavans, D. L. Court, S. Adhya, Switches in bacteriophage lambda development. *Annual review of genetics* **39**, 409-429 (2005).
16. M. Fujita, R. Losick, Evidence that entry into sporulation in Bacillus subtilis is governed by a gradual increase in the level and activity of the master regulator Spo0A. *Genes & development* **19**, 2236-2244 (2005).
17. H. Vlamakis, C. Aguilar, R. Losick, R. Kolter, Control of cell fate by the formation of an architecturally complex bacterial community. *Genes & development* **22**, 945-953 (2008).
18. I. Pastushenko *et al.*, Identification of the tumour transition states occurring during EMT. *Nature* **556**, 463-468 (2018).
19. J. L. McFaline-Figueroa *et al.*, A pooled single-cell genetic screen identifies regulatory checkpoints in the continuum of the epithelial-to-mesenchymal transition. *Nat. Genet.* **51**, 1389-1398 (2019).
20. I. Pastushenko, C. Blanpain, EMT transition states during tumor progression and metastasis. *Trends Cell Biol.* **29**, 212-226 (2019).
21. T. S. Gardner, C. R. Cantor, J. J. Collins, Construction of a genetic toggle switch in Escherichia coli. *Nature* **403**, 339-342 (2000).
22. K. D. Litcofsky, R. B. Afeyan, R. J. Krom, A. S. Khalil, J. J. Collins, Iterative plug-and-play methodology for constructing and modifying synthetic gene networks. *Nat. Methods* **9**, 1077-1080 (2012).
23. D. E. Cameron, J. J. Collins, Tunable protein degradation in bacteria. *Nat. Biotechnol.* **32**, 1276-1281 (2014).
24. S. Klumpp, T. Hwa, Growth-rate-dependent partitioning of RNA polymerases in bacteria. *Proc. Natl. Acad. Sci. USA.* **105**, 20245-20250 (2008).
25. S. Klumpp, Z. Zhang, T. Hwa, Growth rate-dependent global effects on gene expression in bacteria. *Cell* **139**, 1366-1375 (2009).
26. M. Scott, C. W. Gunderson, E. M. Mateescu, Z. Zhang, T. Hwa, Interdependence of cell growth and gene expression: origins and consequences. *Science* **330**, 1099-1102 (2010).
27. C. You *et al.*, Coordination of bacterial proteome with metabolism by cyclic AMP signalling. *Nature* **500**, 301-306 (2013).
28. S. Hui *et al.*, Quantitative proteomic analysis reveals a simple strategy of global resource allocation in bacteria. *Mol Syst Biol* **11**, 784 (2015).
29. M. Basan *et al.*, Overflow metabolism in Escherichia coli results from efficient proteome allocation. *Nature* **528**, 99-104 (2015).
30. X. Dai *et al.*, Reduction of translating ribosomes enables Escherichia coli to maintain elongation rates

during slow growth. *Nat. Microbiol.* **2**, 16231 (2016).
31. D. W. Erickson *et al.*, A global resource allocation strategy governs growth transition kinetics of Escherichia coli. *Nature* **551**, 119-123 (2017).
32. M. Basan *et al.*, A universal trade-off between growth and lag in fluctuating environments. *Nature* **584**, 470-474 (2020).
33. R. Zhang *et al.*, Topology-dependent interference of synthetic gene circuit function by growth feedback. *Nat. Chem. Biol* **16**, 695-701 (2020).
34. C. Tan, P. Marguet, L. You, Emergent bistability by a growth-modulating positive feedback circuit. *Nat. Chem. Biol* **5**, 842-848 (2009).
35. G.-W. Li, D. Burkhardt, C. Gross, J. S. Weissman, Quantifying absolute protein synthesis rates reveals principles underlying allocation of cellular resources. *Cell* **157**, 624-635 (2014).
36. S. H. Strogatz, *Nonlinear dynamics and chaos: with applications to physics, biology, chemistry, and engineering*. (CRC press, 2018).
37. J. L. Cherry, F. R. Adler, How to make a biological switch. *J. Theor. Biol.* **203**, 117-133 (2000).
38. S. Bhattacharya, Q. Zhang, M. E. Andersen, A deterministic map of Waddington's epigenetic landscape for cell fate specification. *BMC Syst. Biol.* **5**, 1-12 (2011).
39. M. Wu *et al.*, Engineering of regulated stochastic cell fate determination. *Proc. Natl. Acad. Sci. USA* **110**, 10610-10615 (2013).
40. C. Liao, A. E. Blanchard, T. Lu, An integrative circuit-host modelling framework for predicting synthetic gene network behaviours. *Nat. Microbiol.* **2**, 1658-1666 (2017).
41. N. Moris, C. Pina, A. M. Arias, Transition states and cell fate decisions in epigenetic landscapes. *Nat. Rev. Genet.* **17**, 693-703 (2016).
42. S. Oehler, E. R. Eismann, H. Krämer, B. Müller-Hill, The three operators of the lac operon cooperate in repression. *EMBO J.* **9**, 973-979 (1990).
43. R. Soldatov *et al.*, Spatiotemporal structure of cell fate decisions in murine neural crest. *Science* **364**, (2019).
44. M. A. Coomer, L. Ham, M. P. H. Stumpf, Noise distorts the epigenetic landscape and shapes cell-fate decisions. *Cell Syst.*, (2021).
45. T. M. Norman, N. D. Lord, J. Paulsson, R. Losick, Memory and modularity in cell-fate decision making. *Nature* **503**, 481-486 (2013).
46. S. K. Aoki *et al.*, A universal biomolecular integral feedback controller for robust perfect adaptation. *Nature* **570**, 533-537 (2019).
47. Y. Li *et al.*, A programmable fate decision landscape underlies single-cell aging in yeast. *Science* **369**, 325-329 (2020).
48. S. Bakshi *et al.*, Tracking bacterial lineages in complex and dynamic environments with applications for growth control and persistence. *Nat. Microbiol.* **6**, 783-791 (2021).
49. J. Wang, L. Xu, E. Wang, Potential landscape and flux framework of nonequilibrium networks: robustness, dissipation, and coherence of biochemical oscillations. *Proc. Natl. Acad. Sci. USA.* **105**, 12271-12276 (2008).
50. J. Wang, K. Zhang, L. Xu, E. Wang, Quantifying the Waddington landscape and biological paths for development and differentiation. *Proc. Natl. Acad. Sci. USA* **108**, 8257-8262 (2011).
51. N. Perrimon, C. Pitsouli, B.-Z. Shilo, Signaling mechanisms controlling cell fate and embryonic patterning. *Cold Spring Harb. Perspect. Biol.* **4**, a005975 (2012).
52. P. Li, M. B. Elowitz, Communication codes in developmental signaling pathways. *Development* **146**, dev170977 (2019).
53. H. E. Johnson, J. E. Toettcher, Signaling dynamics control cell fate in the early Drosophila embryo. *Dev. Cell* **48**, 361-370. e363 (2019).
54. H. Vlamakis, Y. Chai, P. Beauregard, R. Losick, R. Kolter, Sticking together: building a biofilm the Bacillus subtilis way. *Nat. Rev. Microbiol.* **11**, 157-168 (2013).
55. C. García-Jiménez, C. R. Goding, Starvation and pseudo-starvation as drivers of cancer metastasis through translation reprogramming. *Cell Metab.* **29**, 254-267 (2019).
56. J. Davies, Using synthetic biology to explore principles of development. *Development* **144**, 1146-1158 (2017).
57. G. Schlissel, P. Li, Synthetic developmental biology: understanding through reconstitution. *Annu. Rev. Cell Dev. Biol.* **36**, 339-357 (2020).
58. I. Zorzan, A. R. López, A. Malyshava, T. Ellis, M. Barberis, Synthetic designs regulating cellular transitions: Fine-tuning of switches and oscillators. *Curr. Opin. Syst. Biol.* **25**, 11-26 (2021).
59. N. Shakiba, R. D. Jones, R. Weiss, D. Del Vecchio, Context-aware synthetic biology by controller design: Engineering the mammalian cell. *Cell Syst.* **12**, 561-592 (2021).
60. J. Negrete, Jr., A. C. Oates, Towards a physical understanding of developmental patterning. *Nat. Rev. Genet.* **22**, 518-531 (2021).

61. S. Datta, N. Costantino, D. L. Court, A set of recombineering plasmids for gram-negative bacteria. *Gene* **379**, 109-115 (2006).
62. C. Engler, R. Kandzia, S. Marillonnet, A one pot, one step, precision cloning method with high throughput capability. *PloS one* **3**, e3647 (2008).
63. F. C. Neidhardt, P. L. Bloch, D. F. Smith, Culture medium for enterobacteria. *J. Bacteriol.* **119**, 736-747 (1974).
64. H. Zheng *et al.*, General quantitative relations linking cell growth and the cell cycle in Escherichia coli. *Nat. Microbiol.* **5**, 995-1001 (2020).
65. A. J. Meyer, T. H. Segall-Shapiro, E. Glassey, J. Zhang, C. A. Voigt, Escherichia coli "Marionette" strains with 12 highly optimized small-molecule sensors. *Nat. Chem. Biol* **15**, 196-204 (2019).
66. M. Martin, Cutadapt removes adapter sequences from high-throughput sequencing reads. *EMBnet j.* **17**, 10-12 (2011).
67. B. Langmead, S. L. Salzberg, Fast gapped-read alignment with Bowtie 2. *Nat. Methods* **9**, 357-359 (2012).
68. P. Danecek *et al.*, Twelve years of SAMtools and BCFtools. *Gigascience* **10**, giab008 (2021).
69. A. E. Borujeni, J. Zhang, H. Doosthosseini, A. A. Nielsen, C. A. Voigt, Genetic circuit characterization by inferring RNA polymerase movement and ribosome usage. *Nat. Commun.* **11**, 1-18 (2020).

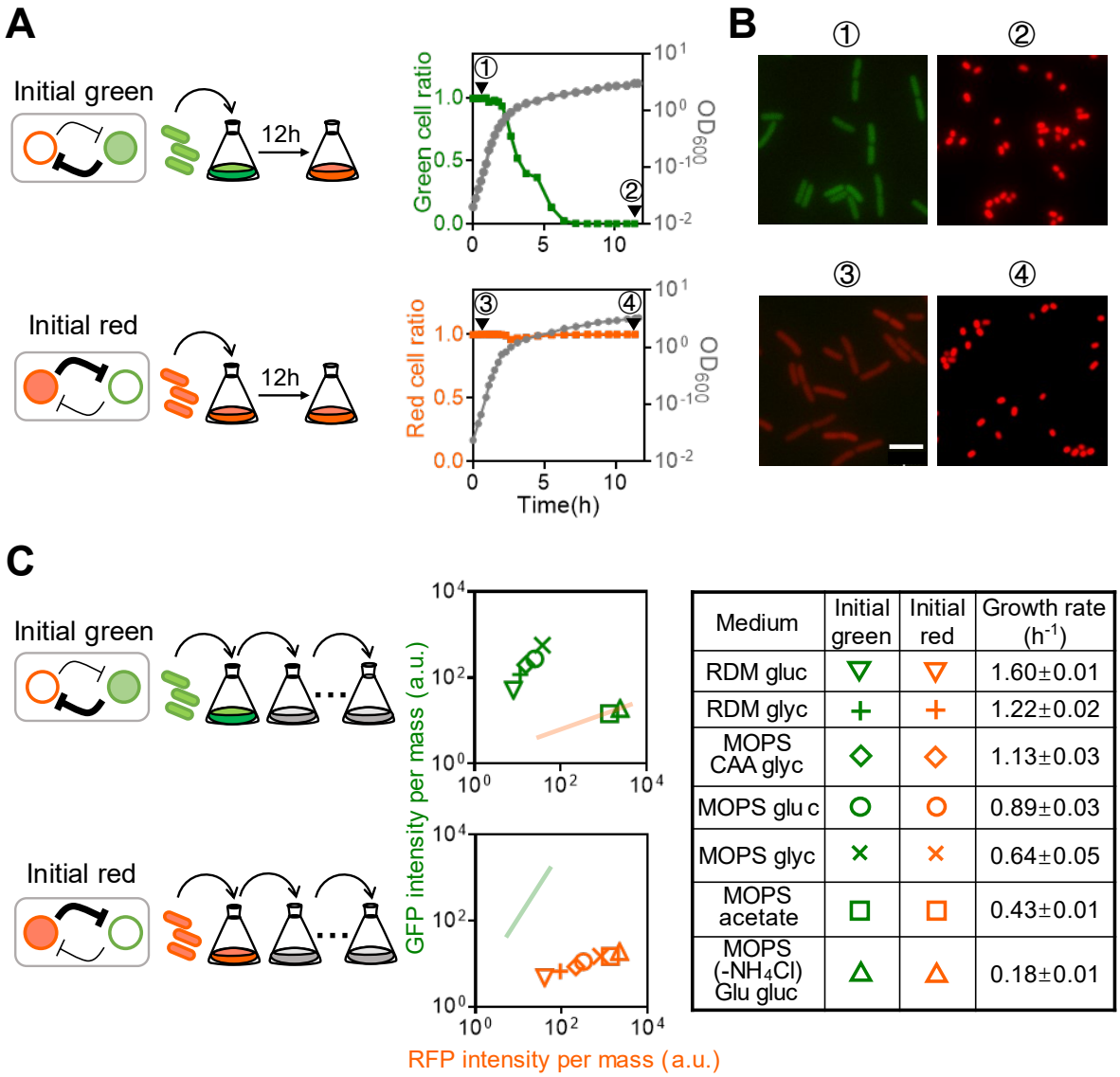

Medium	Initial green	Initial red	Growth rate (h^{-1})
RDM gluc	▽	▽	1.60±0.01
RDM glyc	+	+	1.22±0.02
MOPS CAA glyc	◇	◇	1.13±0.03
MOPS glu c	○	○	0.89±0.03
MOPS glyc	×	×	0.64±0.05
MOPS acetate	□	□	0.43±0.01
MOPS (-NH_4Cl) Glu gluc	△	△	0.18±0.01

Fig. 1: Cellular physiology dependent state determination of a mutually repressive synthetic circuit.

(A) The cell state kinetics during bulk culture growth, with cells initialized as two mutually repressive states: high LacI/GFP and low TetR/RFP (green state), or low LacI/GFP and high TetR/RFP (red state). To better discriminate the phenotypic states, we normalized the fluorescent signals by a separatrix in the scatter plot of GFP intensity per mass against RFP intensity per mass generated at each time point throughout the cell culture and thereby defined the cell ratio in the green state (Fig. S2). Starting with cells in the green state (①), the green cell ratio decreases (the red cell ratio increases, Fig. S2) until all cells transit into the red state (②), as the growth rate drops due to nutrient depletion of bulk culture. Meanwhile, starting with cells initialized in the red state (③), the red cell ratio keeps constant during the bulk culture growth, so that cells maintain in the red state (④). **(B)** Representative microscopic images of cells at different times (①-④), the scale bar shows 5 μm in distance. **(C)** Cell

phenotypic state under different steady-state growth conditions (the growth media are listed, see Table S3 and S4 for details), with two different initial states: initial green state (green symbols) or initial red state (red symbols). Steady-state protein concentrations are given by the fluorescence intensity per mass measured under exponential growth conditions (see SI). Given the two distinct states, we washed the cells and transferred them into a fresh medium without an inducer. Successive dilutions were carried out until the fluorescence intensity level varied less than 5% for each cell population so that the cells were maintained in steady-state growth. The mutual repressive circuit loses its bistability in slow-growth conditions ($\lambda < 0.5\ h^{-1}$).

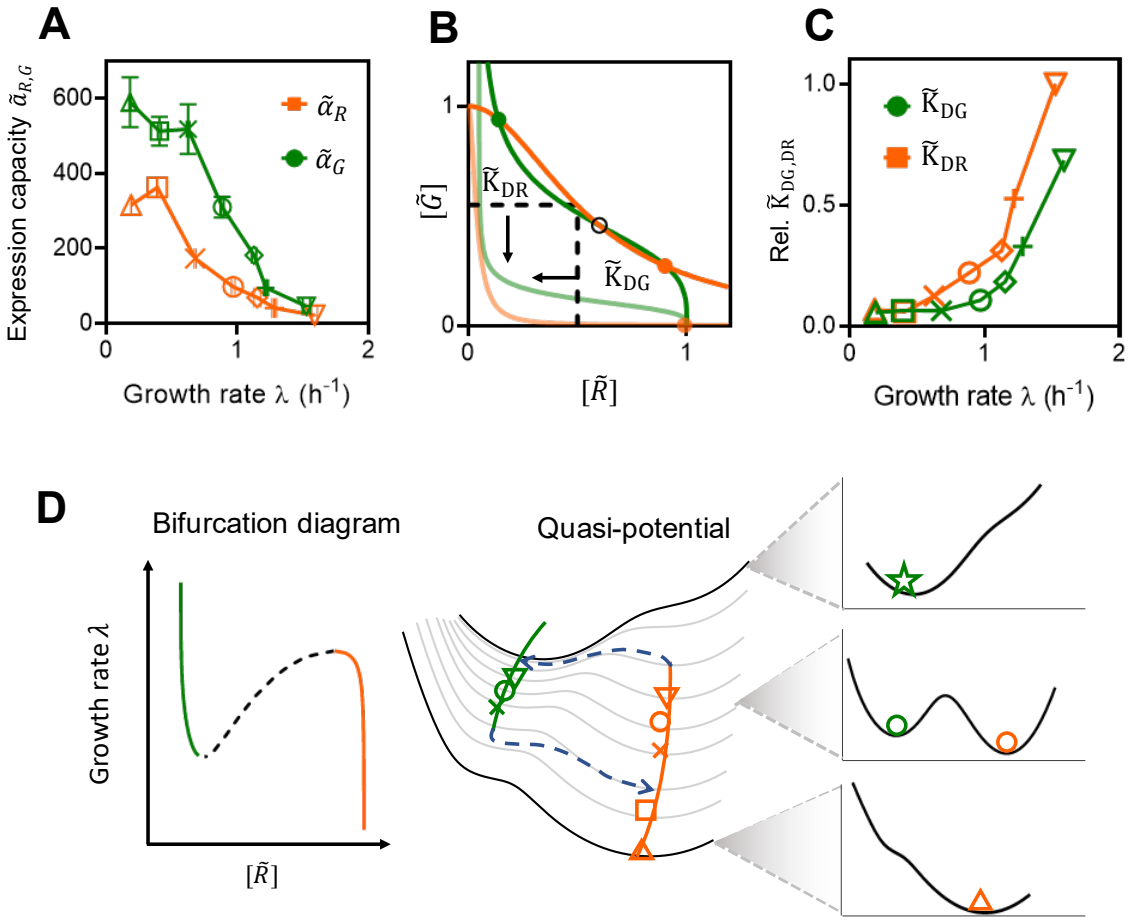

Fig. 2: Cell growth-induced bifurcation and cell fate decision.

(A) Growth-dependent expression capacity of constitutively expressed TetR (red symbols) and LacI (green symbols), respectively. Two separated parts that constitutively expressed *tetR* and *lacI* with C-terminal *sfgfp* fusion were used for the measurement of their corresponding expression capacity (Fig. S5A). Different symbols correspond to growth media listed in Fig. 1B. Data represent the mean ± SD for at least three biological replicates (Table S6). **(B)** Illustration of fix points and their stability by nullclines plot for the mutually repressive system. The unbalanced variations of repression thresholds result in the two nullclines experiencing a transition from three fix points (by two solid lines, with two stable states marked as solid dots and one unstable state marked as an open circle) to a single point (by two transparent lines, with only one stable state marked as a transparent dot). **(C)** Relative repression thresholds in units of gene expression capacity as a monotonically increasing function of growth rate. **(D)** Schematic of quasi-potential landscapes under different growth rates. Cell fate decision is coordinated through growth-rate-dependent parameters by invoking growth rate λ as control parameter in a bifurcation diagram (left panel, solid lines represent the ensemble of stable steady-states, the dashed line indicates the ensemble of unstable steady-states, i.e., the saddle

points). The evolution of the calculated quasi-potential landscape (see SI) in varying the cell growth rate is given in the middle panel (symbols represent different conditions indicated in Fig. 1C). At critical growth rate, a saddle-node bifurcation takes place (dashed blue lines in the right panel) when one stable steady-state is destabilized and shifts to the other one.

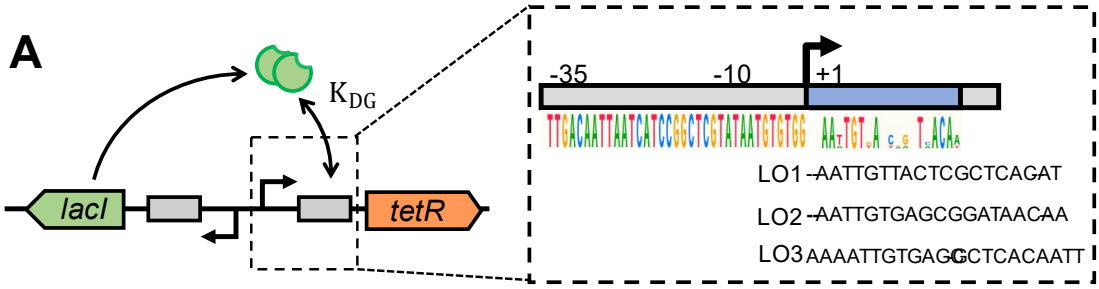

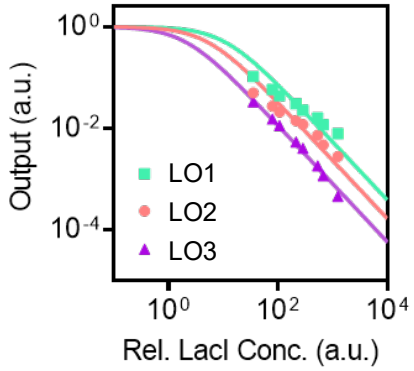

Operator	Repression threshold K_{DG}
LO1	10.5±1.6
LO2	5.0±0.7
LO3	2.0±0.2

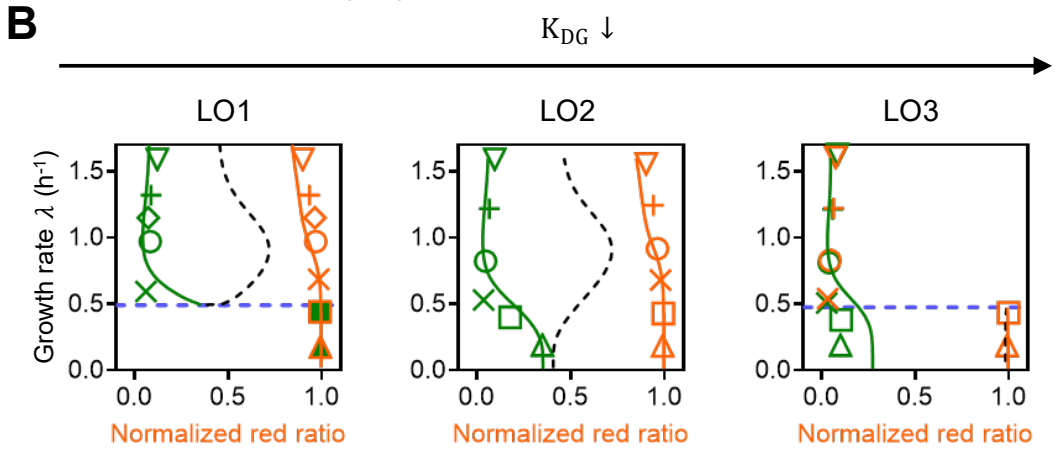

Fig. 3: Titration of the repression threshold shifts the phenotypic bifurcation diagram. **(A)** Three representatives of synthetic binding sites for transcription factor LacI to vary the repression threshold K_{DG} (Table S10). Quantification of repression response curves confirms the titration of repression threshold without affecting the cooperativity of the repression response curves (Fig. S8). The inputs and outputs are obtained by measuring the expression level of fluorescence reporter mVenus (see Materials and Methods). Symbols represent the experimental data and solid lines donate parameter fitting lines with fixed Hill coefficient. The relative values of the repression threshold and standard deviation are provided in the table. **(B)** Bifurcation diagrams of mutually repressive systems with different repression thresholds K_{DG}, using growth rate as the key control parameter. The phenotypic state is quantified as the normalized red ratio, which is defined as the ratio of GFP fluorescent intensity to the sum of GFP and RFP fluorescent intensity under different growth conditions (Table S5 and S7).

Different symbols are given in Fig. 1C. Solid lines indicate the ensembles of theoretically calculated protein concentrations at stable steady-state using the same normalization method as the experimental data, while black dashed lines point out the calculated saddle points that can hardly be measured experimentally. The quasi-potential landscape under fast growth (λ =1.60 h^{-1}) and slow growth (λ = 0.18 h^{-1}) are indicated for each of the design in Fig. S9.

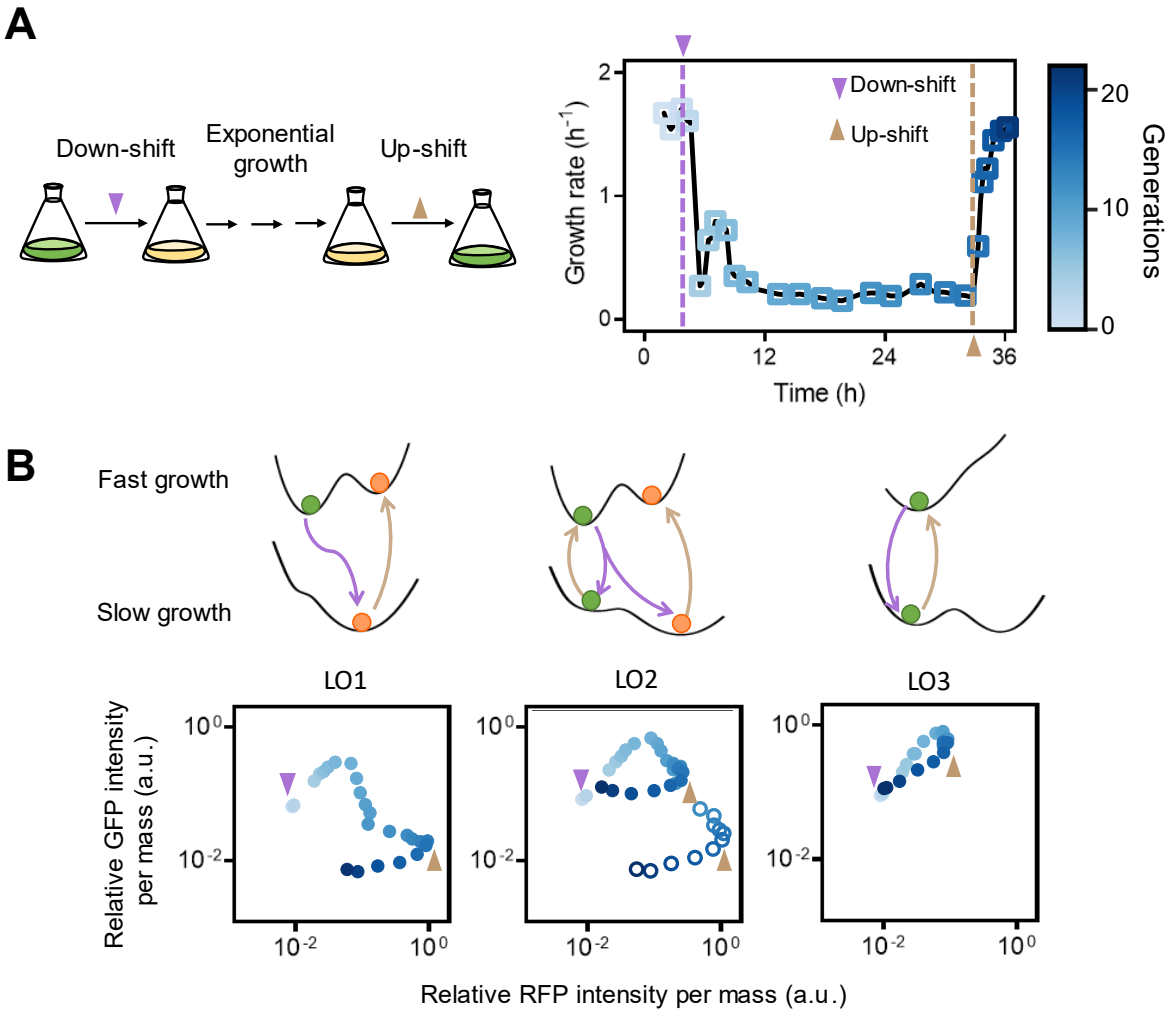

Fig. 4: Irreversible and reversible cell fate determination.

(A) Illustration of growth down-shift from RDM glucose medium to MOPS (-NH_4Cl) glutamate glucose medium and up-shift experiments (see Materials and Methods), and the corresponding instantaneous growth rate. The violet down-arrow indicates the time at which the rich medium is depleted, and the yellow up-arrow refers to the moment the nutrient up-shift is performed. The colors of symbols in the right panel correspond to the number of generations since t=0, which is determined by counting the doubling of cell mass (see Materials and Methods). After nutrient down-shift, the instantaneous growth rate λ drops abruptly, followed by rapid recovery, and overshot until reaches around 0.9 h^{-1} and then further slows down towards the steady-state growth rate (~0.18 h^{-1}) in the after-shift medium. During the growth up-shift, the instantaneous growth converged to the final rate in several hours. The cell growth dynamics are not affected by the different genetic circuits mentioned above, for the kinetics of cell growth were highly consistent among different strains, see Fig. S10.

(B) Trajectories of cell fate determination during growth-shift. The quasi-potential landscapes calculated for fast and slow growth conditions are provided in the top panels. Population

averaged protein concentrations are plotted in a LacI-GFP versus TetR-RFP plane with colours indicating the numbers of generations in the bottom panel. The solid circles and hollow ones refer to two subpopulations characterized. Cells exhibit irreversible fate determination through saddle-node bifurcation (LO1, and LO2 hollow circles) and reversible ones (LO2 solid circles, and LO3) as well.